

Effect of Stator on Core Loss of the Embedded Combined Magnetic Pole Drive Motor for New Energy Vehicles

Shilong Yan¹, Mingling Gao^{2, *}, Jun Zhang³, Mingjun Xu¹,
Yufeng Zhang¹, and Wei Wang¹

Abstract—To reduce the loss of a drive motor and improve the output efficiency of the drive motor, this paper explores the influencing factors of core loss of an embedded combined magnetic pole drive motor (ECMPDM) for new energy vehicles. The mathematical model of the core loss of the drive motor is established. The monitoring points are selected in different areas of the stator to analyze the distribution of magnetic density, and the correctness of the model is preliminarily verified. Taking the motor core loss as the primary objective of optimization, the multi-objective optimization of the stator slot structure size is carried out by the response surface analysis method. The average value of the stator core loss and the radial magnetic density amplitude of the B point is taken as the two optimization objectives, and the optimal solution of the model is selected by the Pareto frontier distribution diagram. The optimal stator structure is analyzed, and the core loss value is calculated by three methods and compared with the simulation value. The prototype experiments of the optimized motor are carried out, and the no-load core loss experiment, rated voltage characteristic experiment, and peak power characteristic experiment are carried out, which verify the rationality of the optimized size and structure of the embedded combined magnetic pole drive motor for new energy vehicles and provide a possibility for the analysis of the temperature field of the embedded combined magnetic pole drive motor for new energy vehicles.

1. INTRODUCTION

Permanent magnet synchronous motors for electric vehicle drives have the advantages of small volume, high power density, high efficiency, high integration, and large speed regulation range. However, when the operating temperature of the motor is too high, the permanent magnet will demagnetize; its flux decreases, leading to the increase of armature reaction flux, which will increase the winding loss of the motor; and the increase in loss will affect the temperature rise. Accurate calculation of losses is critical to the safe operation of the motor [1]. Different losses occur during the operation of motors, including core losses of stator and rotor, copper losses of armature winding, eddy current losses of permanent magnet, and mechanical losses [2]. Because the core loss is closely related to the magnetic flux density and frequency of the motor, and the magnetic flux density distribution of the motor is complicated, it is difficult to calculate the core loss accurately in the study of various loss calculations. Therefore, it is of great significance to study the influencing factors of stator core loss to reduce the total loss of motor, improve efficiency, and improve the performance of motor [3].

Many scholars have done a lot of research on core loss. References [4–6] proposed an improved core loss calculation method for a built-in permanent magnet synchronous motor. Based on the armature

Received 11 September 2022, Accepted 7 December 2022, Scheduled 17 December 2022

* Corresponding author: Mingling Gao (gml_3437@sina.com).

¹ School of Transportation and Vehicle Engineering, Shandong University of Technology, Xincun West Road, Zhangdian District, Zibo, Shandong Province, China. ² School of Computer Science and Technology Shandong University of Technology Xincun West Road, Zhangdian District, Zibo, Shandong Province, China. ³ Shandong Tangjun Ouling Automobile Manufacturing Co., Ltd Tangjun Ouling Road, Zichuan District, Zibo, Shandong Province, China.

reaction principle, the magnetic density distribution of air gap, stator teeth, and the yoke were analyzed; the influence of arc coefficient and grooves per pole on loss was studied; and the core loss of stator teeth was obtained under weak magnetic control. Reference [7] held that the traditional Fourier method based on air gap magnetic density space waveform was not suitable for surface-mounted permanent magnet motors, and proposed to use the method of magnetic density change with time waveform to calculate the core loss. Reference [8] proposed a new method to calculate the core loss of permanent magnet synchronous motor (PMSM) under space vector pulse width modulation (SVPWM) excitation considering magnetic saturation and cross-coupling. Based on the magnetic field distribution of the motor, the core loss analysis model was used to calculate the stator core loss. Reference [9] proposed a stator core shape design method to improve the power density of permanent magnet motors by keeping the winding area unchanged and not reducing the torque. Reference [10] studied the core loss in the stator region of a permanent magnet synchronous motor, the magnetic field characteristics in the load area, and variations in core losses caused by changes in these areas. It was concluded that the loss of stator core is mainly concentrated at the stator yoke, and the loss of the stator under rated load conditions was greater than that under no-load conditions. Reference [11] studied the waveforms of the magnetic density at different positions of the core during no-load operation and obtained the distribution of different losses of the core. It was found that the stator core loss was mainly distributed at the junction of the tooth part and the yoke part, the yoke part, and the tooth body area. Reference [12] studied the iron consumption characteristics of a high-efficiency lightweight variable leakage permanent magnet motor under different operating conditions. The mathematical relationship between magnetic density and iron consumption of variable leakage permanent magnet motor was derived, and the influence of parameters in magnetic leakage area on iron consumption was analyzed by using the response surface method.

To reduce the loss of the drive motor and improve the output efficiency of the drive motor, this paper explores the influencing factors of core loss of the embedded combined magnetic pole drive motor for new energy vehicles. The mathematical model of the driving motor on the core loss is established. It can be known from the mathematical model that the distribution of magnetic density in iron core affects the core loss. Therefore, the monitoring point is selected at the typical position of the stator to analyze the distribution of magnetic density. A certain point of the stator tooth top is selected as the analysis point, and different stator slot geometries are analyzed. The first optimization goal is to reduce the core loss of the motor, and the slot type suitable for the motor is selected. The response surface analysis method is used to optimize the multi-parameters of the stator slot. The radial magnetic density amplitude at a certain point of the stator tooth top and the average value of stator core loss are selected as the two optimization objectives. The Pareto frontier distribution map is obtained by solving the problem, and the optimal solution of the optimization model is selected. The optimized model is simulated and analyzed to get the magnetic density of each monitoring point. Three methods are used to process the magnetic density waveform and analyze the stator magnetic density waveform under no-load conditions. The core loss under three methods is obtained. The prototype of the drive motor is made to verify.

2. STRUCTURE AND CORE LOSS ANALYSIS OF THE ECMPDM

2.1. The Structure of the ECMPDM

In this paper, a permanent magnet synchronous motor with a new rotor structure is proposed. The common loss analysis method is used to analyze the core loss of the new structure. The analysis method is applicable to most permanent magnet motors. The new energy vehicle with the ECMPDM is composed of two parts, the stator and rotor. The rotor part is composed of a combined magnetic pole and a rotor core. A parallel magnetic circuit is formed between the main magnetic pole and auxiliary magnetic pole. The advantage is to compensate for the magnetic density depression and make the air gap magnetic density waveform closer to sinusoidal. The structure of the ECMPDM is shown in Figure 1. Table 1 shows the performance index parameters of the ECMPDM.

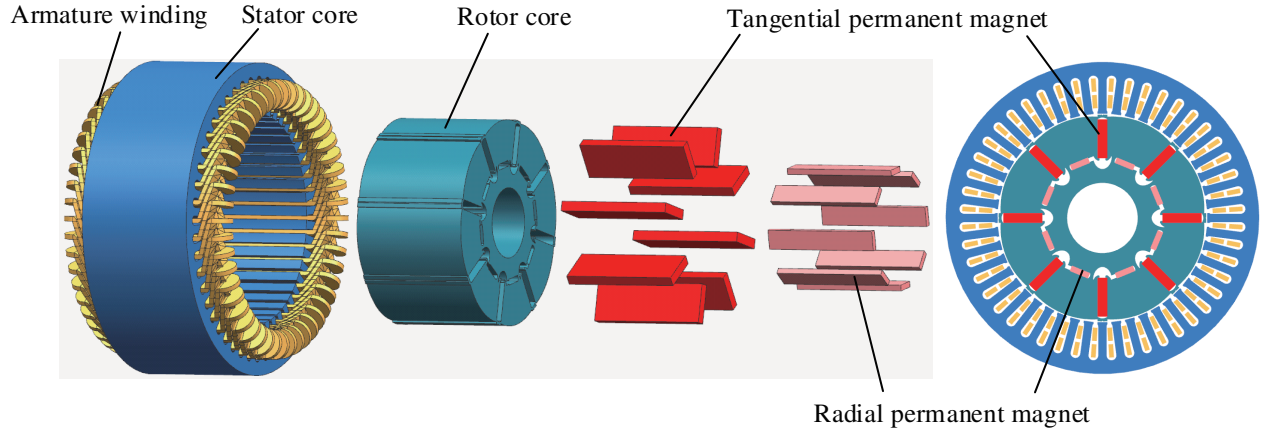


Figure 1. The structure of the ECMPDM.

Table 1. Main parameters of the ECMPDM.

Parameter	Value	Parameter	Value
Rated Power	5 kW	Rated torque	15.9 N × m
Rated voltage	72 V	Number of Phases	3
Rated speed	3000 r/min	Number of Poles	8

2.2. Calculation Model of Core Loss for the ECMPDM

The basic core loss of the stator and rotor is produced by the change of the main magnetic field in the core. Bertotti decomposed core loss into three parts: hysteresis loss, eddy current loss, and additional loss [13]. Because the main magnetic field of the ferromagnetic material can be alternating magnetization, such as in the stator and rotor yoke, it can also be rotational magnetization, such as that occurring in the yoke of the stator or rotor. For alternating magnetization, Bertotti proposed an expression for the iron consumption model:

$$\begin{aligned}
 P_{Fe} &= P_h + P_e + P_{ex} \\
 &= k_h f B_{Fe}^2 + k_e (f B_{Fe})^2 + k_{ex} (f B_{Fe})^{1.5}
 \end{aligned}
 \tag{1}$$

where k_h is the hysteresis loss coefficient, k_e the eddy current loss coefficient, k_{ex} the additional loss correction factor, f the frequency, and B_{Fe} the magnitude of the magnetic density.

When the magnetic flux density waveform changes into the arbitrary waveform, the magnetic flux density vector is usually decomposed into radial component and tangential component. The expression of core loss of magnetic flux density waveform under the change of non-sinusoidal magnetic flux density waveform is as follows:

$$\begin{aligned}
 P_{Fe} &= k_h f \int_0^T \left[\left(\frac{dB_{Fer}(t)}{dt} \right)^2 + \left(\frac{dB_{Fet}(t)}{dt} \right)^2 \right] dt + k_e f^2 \int_0^T \left[\left(\frac{dB_{Fer}(t)}{dt} \right)^2 + \left(\frac{dB_{Fet}(t)}{dt} \right)^2 \right] dt \\
 &\quad + k_{ex} f^{1.5} \int_0^T \left[\left(\frac{dB_{Fer}(t)}{dt} \right)^{1.5} + \left(\frac{dB_{Fet}(t)}{dt} \right)^{1.5} \right] dt
 \end{aligned}
 \tag{2}$$

According to Equation (2), the core losses obtained by different magnetic density analysis methods are different, so it is necessary to simulate and analyze the magnetic field before calculating the stator core loss. The distributions of magnetic fields are different in different areas of the stator core, so it is impossible to calculate all internal points to obtain the whole stator core loss. Therefore, the feature points are selected in different areas of the stator, and the magnetic field analysis is carried out for each feature point in turn [14].

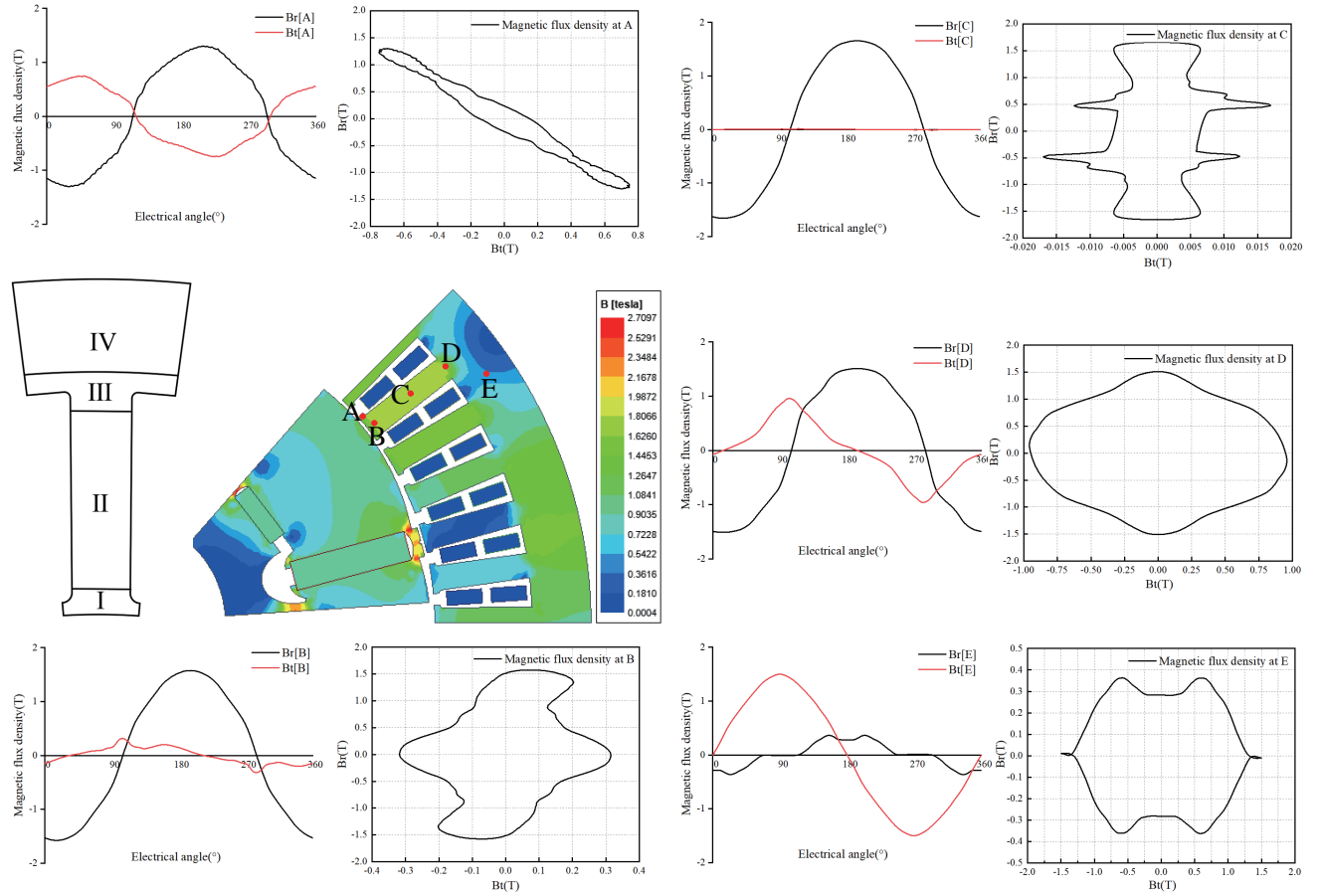


Figure 2. Magnetic density cloud diagram of drive motor and change of magnetic density at monitoring points A, B, C, D, and E.

The stator core is divided into four areas: tooth top, tooth middle, tooth root, and yoke. Take points A and B at the top of the teeth, point C at the middle of the teeth, point D at the root of the teeth, and point E at the yoke of the teeth, as shown in Figure 2. The magnetic density waveforms at different positions of the stator can be obtained by analyzing the magnetic density of the selected position points. Figure 2 shows the decomposition and elliptical magnetic field diagrams of radial and tangential magnetic densities under no load at various locations. At the top of the teeth, the teeth and the yoke of the stator, the change of the magnetic density is not sinusoidal, so the influence of the rotating magnetic field on the core loss of the stator must be considered in the loss calculation. The amplitude difference between tangential and radial magnetic density components at five locations is large. The radial component of magnetic density is larger than the tangential component in the direction from tooth root to the tooth tip and point D located at the junction of the stator teeth and the yoke, and the radial component of magnetic density starts to rise. The tangential component of the magnetic density at point E is larger than the radial component.

According to the EMF balance equation of induction motor in electro-mechanics:

$$\Phi_m = \frac{E_s}{4.44fN_s k} \quad (3)$$

where Φ_m is the main flux, E_s the induced EMF of the stator winding, f the motor operating frequency, N_s the number of turns in series per phase of the winding, and k the fundamental wave winding factor. When the basic parameters of the motor are determined, the main flux will not change as long as the supply voltage of the motor remains unchanged.

3. THE STATOR OPTIMIZATION OF THE ECMPDM

In either operating state, the stator core loss of the motor accounts for a large proportion of the total core loss. Therefore, a reasonable stator structure can reduce the loss of the stator core and then reduce the total core loss, to improve the output efficiency of the motor. With the optimization goal of reducing the total core loss, the relationship between the magnetic density and core loss of the stator B point is analyzed.

By analyzing the flux density of the monitoring points in each area of the stator, it can be seen that the magnetic density at the top of the tooth is most affected by harmonics, and the radial magnetic density is the main component of the magnetic density at the top of the tooth. The tangential component of magnetic density at point A accounts for a large proportion, while the influence of the radial magnetic density is small. The radial magnetic density amplitude of point B is larger than that of point A, and the radial magnetic density has the most important effect on harmonics. So point B is selected to analyze the change of the top magnetic density. Therefore, the influence of the stator cores silicon steel material and the dimensions of stator slot on the magnetic density at point B and the Fourier decomposition of the magnetic density at point B are analyzed.

The evaluation of magnetic flux density is usually expressed in terms of the distortion rate of magnetic flux density:

$$THD = \frac{\sqrt{B_3^2 + B_5^2 + B_7^2 + L + B_n^2}}{B_1} \times 100\% \tag{4}$$

where B_1 is the fundamental wave amplitude, and B_n is the n th harmonic amplitude.

3.1. The Selection of Stator Core Silicon Steel Material

The material and brand of silicon steel sheet selected for the stator core will have an important influence on core loss [15, 16]. Under the condition of the no-load and rated load of the motor, four different types of silicon steel plates, i.e., DW310_35, DW315_50, DW360_50, and DW465_50, are selected in this paper for core loss calculation, and the variation laws of radial magnetic density and Fourier decomposition of B point on stator tip are analyzed. These special steel grades are non-oriented silicon steel sheets. The magnetic permeability of non-oriented silicon steel sheets is basically the same in all directions, which has the advantages of low core loss and good magnetization. The greater the grade of silicon

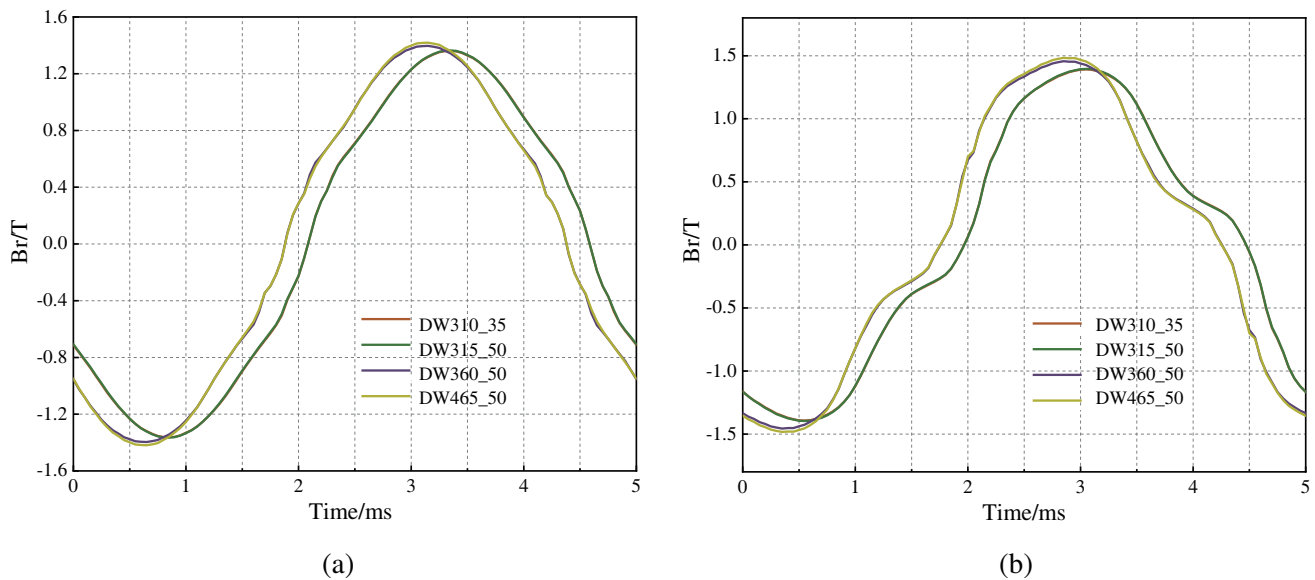


Figure 3. Radial magnetic density waveform. (a) Radial magnetic flux waveform at point B under no-load conditions. (b) Radial magnetic flux waveform at point B under rated load.

steel sheet is, the more core loss it produces. Figure 3 shows the radial flux density waveform at point B under no-load and rated load conditions. DW310_35 and DW315_50 have similar material properties, so their curves are highly coincident. The amplitudes of radial magnetic density at point B of different materials are almost the same. Under no-load conditions, the waveform of magnetic density at point B tends to be sinusoidal. With the increase of load, the sinusoidal property of the radial magnetic density at stator teeth becomes worse and worse.

Table 2 is the Fourier decomposition of the radial magnetic density at point B of the stator tooth top under different silicon steel materials. It can be seen from the Fourier decomposition of magnetic density at stator tooth top under different operating conditions in the table that the fundamental wave content of magnetic density at stator tooth top accounts for the main proportion, and the harmonic content is relatively small. After the 11th harmonic, the harmonic magnitude is 10^{-2} times, and the influence on core loss can be neglected basically. When the material remains unchanged, the basic wave content of magnetic density decreases with the increase of load, but the decreasing trend is not obvious, and the harmonic content increases. At the same time, the stator material is different; the input voltage is the same; and the peak value achieved by the magnetic density is close. The correctness of the variation rule of the fundamental wave content of the tooth crest in Equation (3) is verified.

Figure 4 shows the change of stator core loss of different silicon steel materials under no-load conditions. When the selected silicon steel plate grade is larger, the stator core loss is also larger.

Table 2. Fourier decomposition of the radial magnetic density of point B under different silicon steel materials.

Parameter	DW310_35 (T)		DW315_50 (T)		DW360_50 (T)		DW465_50 (T)	
	No-load	Rated load	No-load	Rated load	No-load	Rated load	No-load (T)	Rated load
1	1.367	1.353	1.365	1.354	1.397	1.424	1.407	1.440
3	0.034	0.143	0.029	0.147	0.019	0.132	0.065	0.141
5	0.049	0.116	0.050	0.115	0.041	0.128	0.040	0.129
7	0.031	0.025	0.031	0.023	0.033	0.022	0.029	0.019
9	0.012	0.012	0.012	0.012	0.009	0.013	0.007	0.014
11	0.002	0.004	0.003	0.004	0.003	0.005	0.001	0.005
13	0.001	0.003	0.002	0.003	0.001	0.004	0.004	0.004
15	0.002	0.005	0.002	0.004	0.002	0.007	0.005	0.005

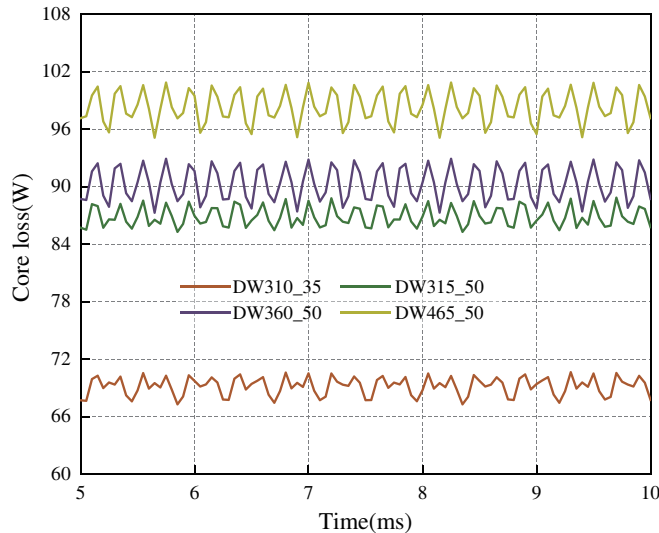


Figure 4. The stator core loss of different silicon steel materials under no-load conditions.

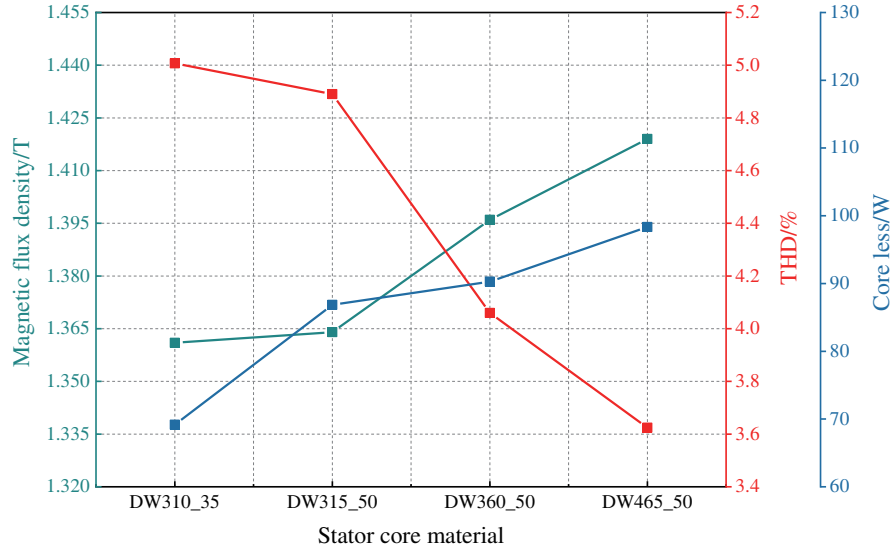


Figure 5. Relationship between the stator core loss under different silicon steel materials and the radial magnetic density of point B and its distortion rate.

DW310.35 has the lowest core loss among the four selected materials. Figure 5 shows the relationship between stator core loss and B-point radial magnetic density and its distortion rate under different silicon steel materials. With the increase of the stator material grade, the stator core loss increases. DW310.35 is selected as the core material of the motor in the case of ensuring that the iron exhaustion is small.

3.2. Multi-Objective Optimization of the Stator Slot Based on Latin Hypercube Sampling

The structure parameters of the permanent magnet drive motor stator are interconnected, and the performance effects of each parameter on the motor are complex and changeable. Therefore, it is necessary to establish a mathematical model between the design variables of a stator slot structure and several influencing variables of the performance of the drive motor and optimize it with a reasonable optimization algorithm based on the mathematical model.

In this paper, the sample point acquisition-Pareto frontier solution method is used for multi-objective optimization of the stator slot. When there are too many design variables, the use of the orthogonal experimental method will cause too many sampling points and reduce the optimization efficiency. Therefore, the selection of the Latin hypercube sampling method can cover the entire sampling space with fewer sampling points, greatly shorten the optimization time, and the use of the Latin hypercube sampling method can make the distribution of sampling points more uniform [17, 18].

Stator slot parameters such as H_{s0} , H_{s1} , H_{s2} , B_{s0} , B_{s1} , and B_{s2} are selected as design variables. Figure 6 shows the diagram of the stator slot parameters. The radial magnetic density of the stator monitoring point B of the drive motor and the core loss of the stator are two optimization objectives. The constraints for each design variable are shown in Table 3.

Table 3. Constraints on design variables.

Design variable	Constraint condition	Design variable	Constraint condition
H_{s0}	$0.5 \text{ mm} \leq H_{s0} \leq 2 \text{ mm}$	B_{s0}	$1.5 \text{ mm} \leq B_{s0} \leq 3 \text{ mm}$
H_{s1}	$0.5 \text{ mm} \leq H_{s1} \leq 2 \text{ mm}$	B_{s1}	$2 \text{ mm} \leq B_{s1} \leq 4 \text{ mm}$
H_{s2}	$13 \text{ mm} \leq H_{s2} \leq 17 \text{ mm}$	B_{s2}	$4 \text{ mm} \leq B_{s2} \leq 6.5 \text{ mm}$

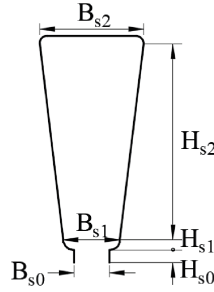


Figure 6. The diagram of the stator slot parameters.

Under the constraints, the optimization model is used to maximize the radial magnetic density of the stator monitoring point B and minimize the core loss of the stator, which are functions of six design variables.

$$\begin{cases} \max B_{rx}(x_1, x_2, \dots, x_a) \\ \min CL_x(x_1, x_2, \dots, x_a) \end{cases} \quad (5)$$

where B_{rx} is the radial magnetic density amplitude of the stator tooth monitoring point B, and CL_x is the average stator core loss.

Assume that at that stator yoke height stays unchanged and that there are A random variables in an optimization problem, and X_a is any of them.

The distribution function is:

$$Y_a = F_a(X_a) \quad (6)$$

Assuming that the sampling number is B , the longitudinal axis of Y_a is divided into B equal intervals. It is assumed that each variable is independent, and x_{ab} is the b th sampling value of the a th variable. Then the Latin hypercube sampling procedure is as follows [19, 20]:

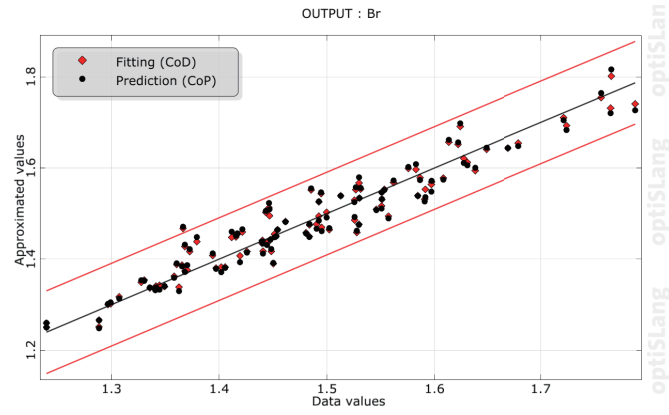
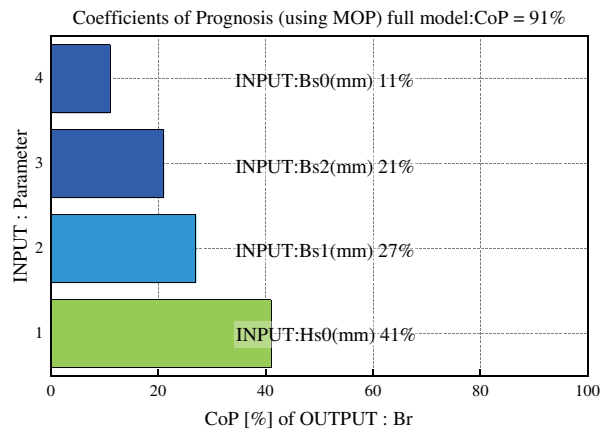
- 1) Generate an $a \times b$ dimension matrix $M_{a \times b}$. Each row of the matrix is a random sequence of (1, B) integers, and m_{ab} is its element in row a and column b .
- 2) Generate an $a \times b$ dimension matrix $N_{a \times b}$. Each element of the matrix is evenly distributed [0, 1], and n_{ab} is its element in row a and column b .
- 3) The $a \times b$ dimensional sampling matrix $Y_{a \times b}$ is calculated, and y_{ab} is its element in row a and column b .

$$y_{ab} = F_a^{-1} \left(\frac{m_{ab} - n_{ab}}{B} \right) \quad (7)$$

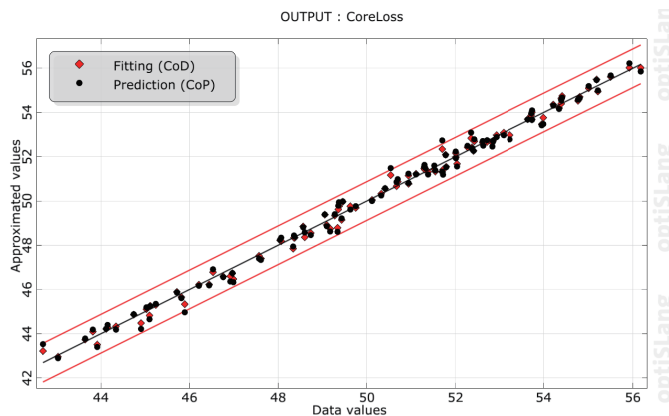
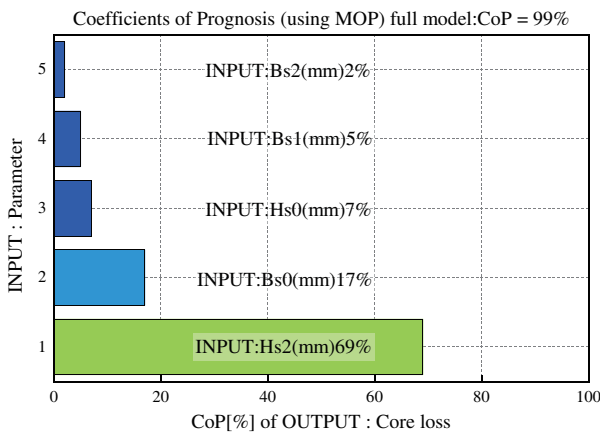
where $a = 1, 2, \dots, A$; $b = 1, 2, \dots, B$.

Finite element simulation is carried out for the optimization model. The prediction model is evaluated by using the COP-Coefficient of Prognosis. The higher the prediction coefficient is, the higher the accuracy of the model is, and the prediction model can be completely equivalent to the real model when $COP = 1$. Figure 7 shows the proportion and residuals of variables in the predictive model. The target prediction coefficient of variables for radial magnetic density B_r is 0.91, and that of variables for the stator core loss is 0.99. Both prediction coefficients are very close to 1, which indicates that the model is effective. According to the residual plot, most points of the prediction model function are related to the model, which indicates that the model function is valid. Variables affecting radial magnetic flux density are H_{s0} , B_{s1} , B_{s2} , and B_{s0} , accounting for 41%, 27%, 21%, and 11%, respectively. Variables affecting core loss are H_{s2} , B_{s0} , H_{s0} , B_{s1} , and B_{s2} , accounting for 69%, 17%, 7%, 5%, and 2%, respectively.

The variables with the top three proportions of B_r and core loss were selected. The two-by-two matching was made for the three main factors, and the effects on the peak of radial magnetic density at point B and the average value of stator core loss were analyzed. Figure 8 shows a fitting surface between the design variable and response value. With the increase of H_{s0} , B_{s2} , and B_{s1} , the radial magnetic density at point B decreases gradually. With the decrease of H_{s2} and H_{s0} and the increase of B_{s0} , the average core loss of the stator decreases gradually. The design variables and response values are nonuniform and nonlinear, so the optimization model has several better solutions.



(a)



(b)

Figure 7. Ratio chart of a predictive model and residual graph. (a) Ratio chart of a predictive model and residual graph about B_r . (b) Ratio chart of a predictive model and residual graph about core loss.

The Pareto optimization provides a means for multi-objective optimization. By solving the Pareto frontier, the three-dimensional surface can be converted into two-dimensional space, which makes it more intuitive to respond to the distribution law of the optimal solution set [21]. Figure 9 is a Pareto frontier distribution obtained from this optimization model. There are six sample points at the Pareto frontier, each of which is an effective solution for the optimization model. The specific values of the design variables and optimization objectives are shown in Table 4.

In the six effective solutions to choose an optimal solution, the parameter matching coefficient K_s

Table 4. The specific values of design variables and optimization objectives in the effective solution.

Serial number	H_{s0} (mm)	H_{s1} (mm)	H_{s2} (mm)	B_{s0} (mm)	B_{s1} (mm)	B_{s2} (mm)	B_r (T)	Core loss (W)
6	0.7625	1.5275	15.46	2.4975	3.55	4.0625	1.777	59.072
10	0.5525	1.0775	16.3	2.9175	3.43	4.1875	1.765	59.096
51	0.8675	0.6875	13.78	2.3775	3.83	4.5125	1.764	57.847
88	0.6875	1.6775	13.14	2.2875	3.17	4.6625	1.622	53.645
98	0.5075	1.6025	14.02	2.8725	2.07	5.5625	1.495	53.032
97	0.5825	0.9875	14.26	2.7225	2.19	6.4625	1.370	52.693

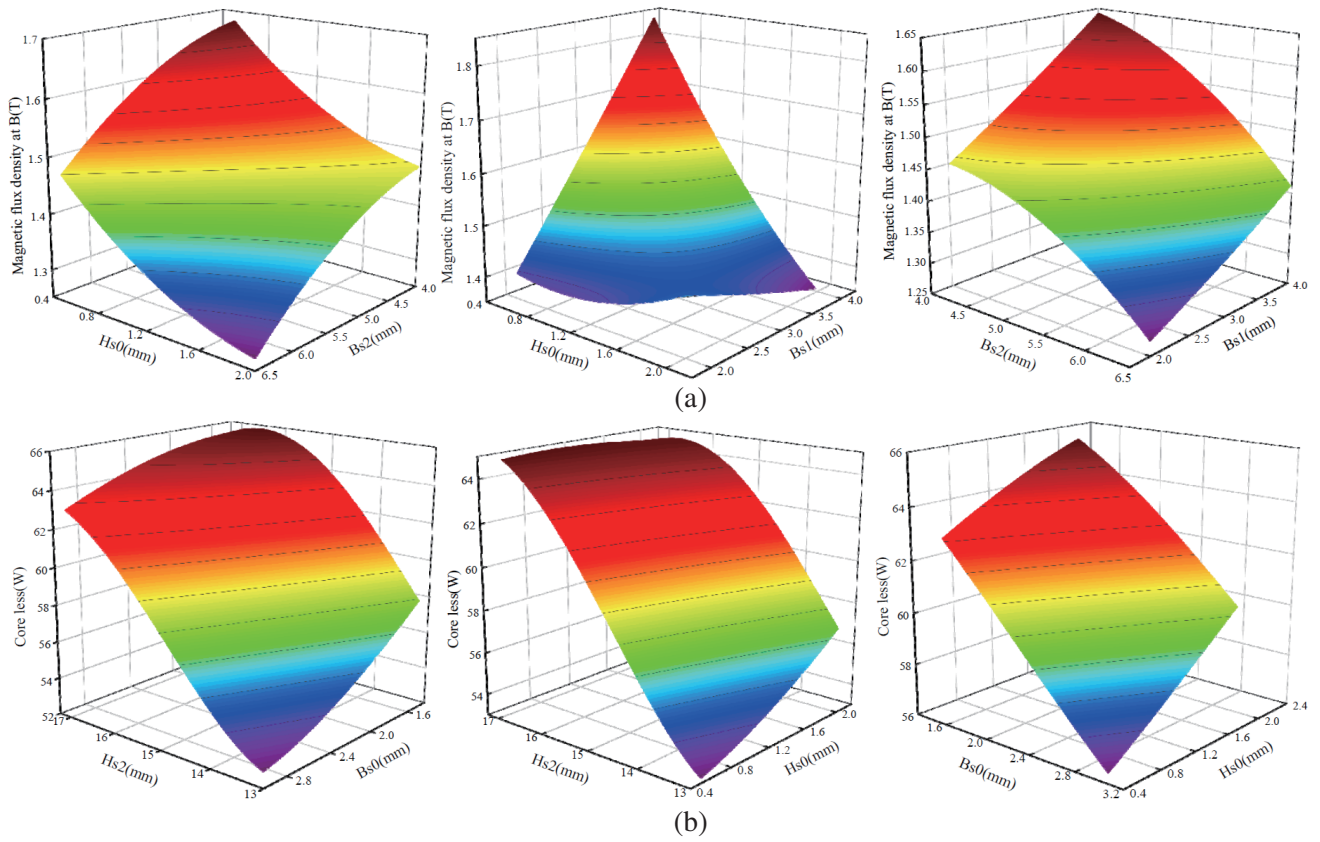


Figure 8. Surface diagram between design variables and response values. (a) Surface diagram of the amplitude of the radial magnetic density at B with variables. (b) Surface diagram of the average value of core loss of the stator with variables.

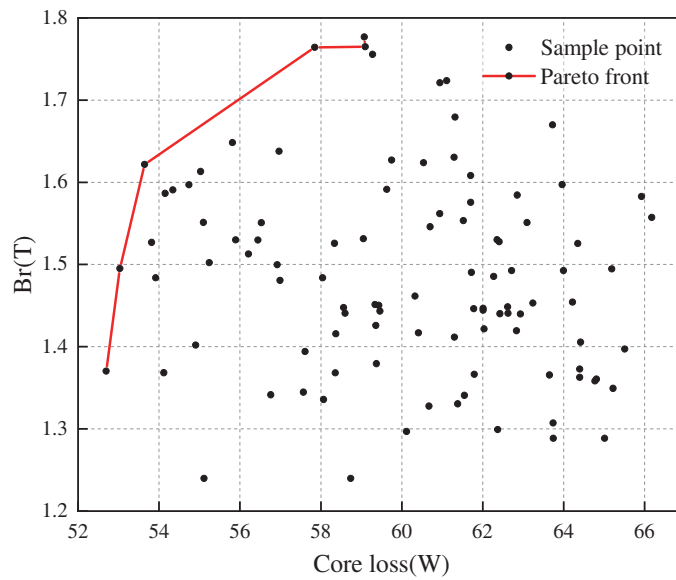


Figure 9. Pareto frontier distribution map.

is introduced, and the two optimization objectives are given different weights. The larger the value of K_s is, the better the output performance is, and the higher the efficiency of the corresponding motor is. The expression is as follows:

$$K_s = C_1 \frac{B_{rx}(x_1, x_2, x_3, x_4, x_5, x_6)}{B_{r0}} - C_2 \frac{CL_x(x_1, x_2, x_3, x_4, x_5, x_6)}{CL_0} \tag{8}$$

where K_s is the parameter matching coefficient, representing the ultimate performance superiority of the motor; C_1 and C_2 are weighted coefficients, and this weight represents the importance of the two optimization objectives. The increase of magnetic flux density will affect the change of core loss, so the weight of magnetic flux density is slightly larger. By preliminary comparison, C_1 and C_2 are selected as 0.64 and 0.34, respectively; B_{r0} is the radial magnetic density amplitude at point B at the initial value of the design variable; CL_0 is the average stator core loss at the initial value of the design variable.

Table 5 shows six valid solutions to obtain the corresponding K_s value according to the above equation. The optimum solution of the optimization model is the 51st sample point, at which point B radial magnetic density is 1.764 T, and the stator core loss is 57.847 W. Table 6 is the final value obtained by combining the actual values of each variable with the actual process. Table 7 shows the comparison between the stator slot size and the optimization objective before and after optimization. Among them, the stator core loss is reduced from 66.81 W to 58.15 W, the radial magnetic density of point B increased from 1.61 T to 1.79 T, and the overall performance of the motor is improved.

Table 5. Values of K_s corresponding to each valid solution.

Sample Points	6	10	51	88	98	97
K_s	0.405	0.4	0.407	0.372	0.321	0.27

Table 6. Optimal solution and the final value of each response variable.

Parameter	Optimum solution (mm)	Final value (mm)
H_{s0}	0.8675	0.87
H_{s1}	0.6875	0.69
H_{s2}	13.78	13.78
B_{s0}	2.3775	2.38
B_{s1}	3.83	3.83
B_{s2}	4.5125	4.51

Table 7. The comparison between the stator slot size and the optimization objective before and after optimization.

Parameter	Before optimization	After optimization
H_{s0}/mm	1	0.87
H_{s1}/mm	1	0.69
H_{s2}/mm	15	13.78
B_{s0}/mm	2	2.38
B_{s1}/mm	3	3.83
B_{s2}/mm	5	4.51
Br/T	1.61	1.79
Core loss/W	66.81	58.15

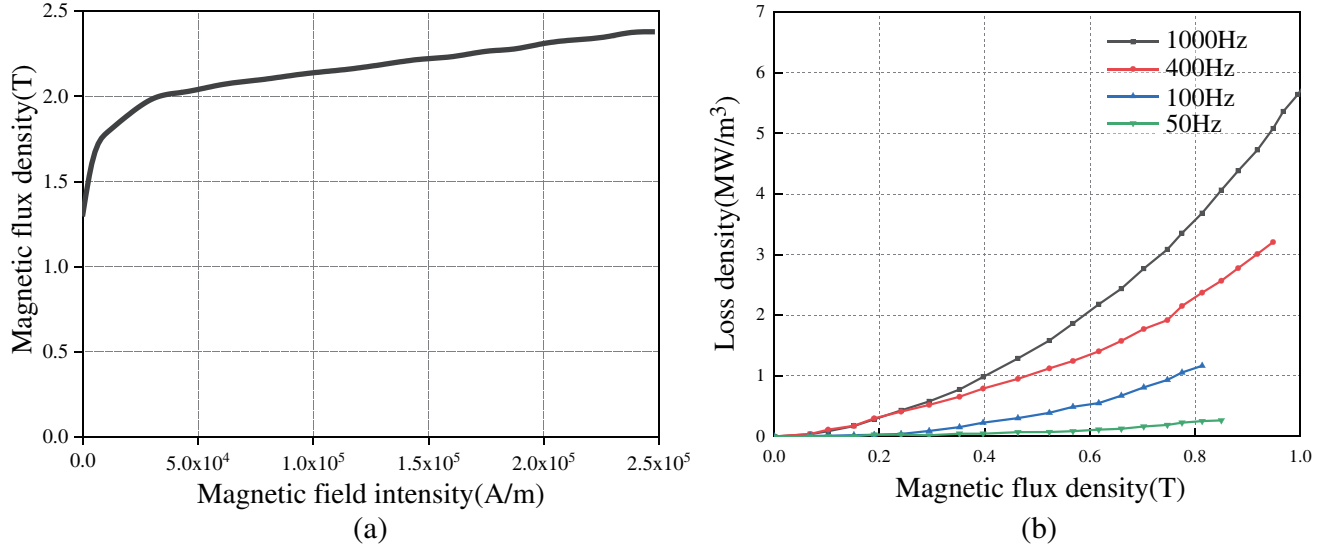


Figure 10. The characteristic curve of DW310-35. (a) B-H curve of DW310-35. (b) B-P curve of DW310-35.

4. CALCULATION OF CORE LOSS OF THE ECMPDM

Before calculating the motor loss, the magnetization curve of the used silicon steel sheet and the loss density curve of the silicon steel sheet at different frequencies are obtained. The material characteristic curve of the silicon steel used in the stator and rotor of the ECMPDM is shown in Figure 10(a). B-P curves at different frequencies of sinusoidal voltages are added to the material properties to fit the existing curves, as shown in Figure 10(b).

According to the B-P curve of the silicon steel sheet, the least square method is used to fit the B-P curve at multiple frequencies to obtain an accurate core loss coefficient [22].

$$f(k_h + k_e + k_{ex}) = \sum_{i=1} \sum_{j=1} [P_{Fe} - (k_h f_i B_{Feij}^2 + k_e f_i^2 B_{Feij}^2 + k_{ex} f_i^{1.5} B_{Feij}^{1.5})]^2 \quad (9)$$

The partial derivatives of the three unknown numbers in Equation (9) are equal to 0 and can be expressed as:

$$\begin{cases} \frac{\partial f(k_h + k_e + k_{ex})}{\partial k_h} = 0 \\ \frac{\partial f(k_h + k_e + k_{ex})}{\partial k_e} = 0 \\ \frac{\partial f(k_h + k_e + k_{ex})}{\partial k_{ex}} = 0 \end{cases} \quad (10)$$

Equation (9) and Equation (10) are derived simultaneously:

$$\begin{cases} \left(\sum_{i=1} \sum_{j=1} f_i^2 B_{Feij}^4 \right) \cdot k_h + \left(\sum_{i=1} \sum_{j=1} f_i^3 B_{Feij}^4 \right) \cdot k_e + \left(\sum_{i=1} \sum_{j=1} f_i^{2,5} B_{Feij}^4 \right) \cdot k_{ex} = \sum_{i=1} \sum_{j=1} p_{ij} f_i B_{Feij}^4 \\ \left(\sum_{i=1} \sum_{j=1} f_i^3 B_{Feij}^4 \right) \cdot k_h + \left(\sum_{i=1} \sum_{j=1} f_i^4 B_{Feij}^4 \right) \cdot k_e + \left(\sum_{i=1} \sum_{j=1} f_i^{3,5} B_{Feij}^{3,5} \right) \cdot k_{ex} = \sum_{i=1} \sum_{j=1} p_{ij} f_i^2 B_{Feij}^2 \\ \left(\sum_{i=1} \sum_{j=1} f_i^{2,5} B_{Feij}^{3,5} \right) \cdot k_h + \left(\sum_{i=1} \sum_{j=1} f_i^{3,5} B_{Feij}^{3,5} \right) \cdot k_e + \left(\sum_{i=1} \sum_{j=1} f_i^3 B_{Feij}^3 \right) \cdot k_{ex} = \sum_{i=1} \sum_{j=1} p_{ij} f_i^{1,5} B_{Feij}^{1,5} \end{cases} \quad (11)$$

Substituting the B-P curve data at each frequency into the equation, $k_h = 0.021$, $k_e = 5.38 \times 10^{-5}$, $k_{ex} = 3.02 \times 10^{-5}$ can be obtained.

It can be seen from the above that core loss is closely related to the magnetic density waveform, and the treatment of the magnetic density waveform will affect the calculation of core loss. According to the analysis of expression of core loss, three methods are used to deal with the magnetic density waveform, and the stator magnetic density waveform under no-load conditions is analyzed. Method 1 uses a sinusoidal equivalent. Assuming that the magnetic density varies according to the sinusoidal law, the peak value of the magnetic density is calculated in Equation (1). Table 8 shows the magnetic density of each detection point. Table 9 shows the core loss of each region obtained by bringing the magnetic density of each detection point into Equation (1). (Note: The loss represented by the monitoring point in the following tables is the total loss per unit mass of the area represented by that point multiplied by the total mass of all the areas.)

Table 8. Peak magnetic density of monitoring points under no-load conditions.

Position	Point B	Point C	Point D	Point E
Peak magnetic density (T)	1.729	1.674	1.420	1.319

Table 9. Method 1 Calculate core loss at rated speed under no-load conditions.

Loss	Tooth tip	Tooth body	Tooth root	Tooth yoke	Stator
Hysteresis loss (W)	1.830	14.072	9.699	9.087	34.688
Eddy current loss (W)	0.938	7.210	4.970	4.655	17.772
Additional Loss (W)	0.028	0.221	0.166	0.161	0.576
Total loss (W)	2.796	21.503	14.835	13.903	53.036

Method 2 adopts the radial tangential component. The magnetic density is decomposed into radial and tangential magnetic density, as shown in Figure 11. Assuming that both change according to the sinusoidal law, and the peak values of both are calculated in Equation (2). Table 10 shows the core loss of each region obtained by substituting the radial and tangential components of the magnetic density of each measurement point into Equation (2).

Table 10. Core loss at rated speed under no-load conditions calculated by method 2.

Loss	Tooth tip	Tooth body	Tooth root	Tooth yoke	Stator
Hysteresis loss (W)	1.971	14.0642	12.1102	9.7354	37.880
Eddy current loss (W)	1.010	7.2063	6.205	4.9882	19.410
Additional Loss (W)	0.032	0.2213	0.221	0.1829	0.657
Total loss (W)	3.013	21.4918	18.5362	14.9065	57.947

Method 3 uses the Fourier decomposition. The radial and tangential components of the magnetic density are decomposed by the Fourier transform, and then the peak value of each harmonic magnetic density is substituted into Equation (2). Table 11 shows the Fourier decomposition of the radial and tangential components of the magnetic density at each monitoring point. Table 12 shows the core loss of each region obtained by substituting the Fourier decomposition of each point into Equation (2).

Table 13 shows the stator no-load core loss at the rated speed calculated by different methods. Among them, hysteresis loss and eddy current loss account for the main part of core loss, and the value of the additional loss can be ignored. Since the magnetic density waveform of the prototype is not a standard sinusoidal variation, the harmonic analysis is added to the magnetic density curve after Fourier

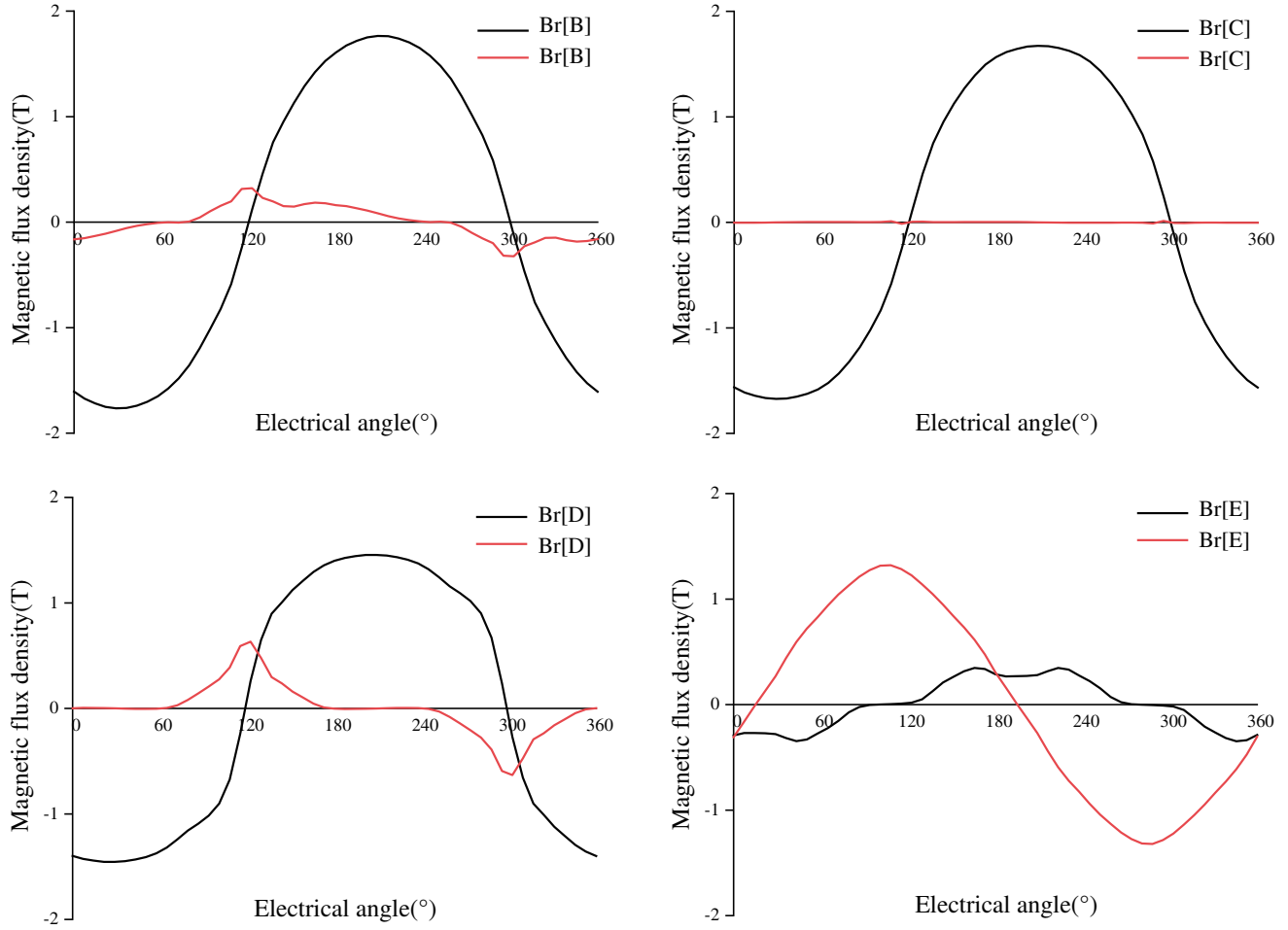


Figure 11. Radial and tangential components after magnetic density decomposition of the monitoring points under no-load conditions.

Table 11. Fourier decomposition of magnetic flux density at monitoring points under no-load conditions.

Parameter	Point B		Point C		Point D		Point E	
	B_r (T)	B_t (T)						
1	1.830	0.272	1.784	0.030	1.600	0.339	0.309	1.250
3	0.134	0.062	0.143	0.001	0.174	0.194	0.040	0.033
5	0.138	0.047	0.133	0.001	0.108	0.051	0.060	0.020
7	0.045	0.035	0.044	0.002	0.045	0.047	0.028	0.009
9	0.003	0.010	0.006	0.002	0.020	0.017	0.005	0.011
11	0.004	0.003	0.001	0.003	0.016	0.002	0.006	0.007
13	0.002	0.004	0.002	0.002	0.004	0.004	0.005	0.003

decomposition, so that the calculated value obtained by Fourier decomposition is greater than that of the sinusoidal equivalent and the radial tangential component.

The simulation value of the optimized stator iron loss is 58.15 W, and the value of the stator iron loss obtained by the second method is 57.947 W. The stator iron loss value obtained by method 2 is closer to the simulation value, so method 2 is more suitable for the loss calculation of this model.

Table 12. Calculation of core loss at rated speed under no-load conditions by method 3.

Loss	Tooth tip	Tooth body	Tooth root	Tooth yoke	Stator
Hysteresis loss (W)	2.096	15.987	12.876	8.658	39.618
Eddy current loss (W)	1.074	8.192	6.598	4.436	20.300
Additional Loss (W)	0.033	0.244	0.218	0.167	0.661
Total loss (W)	3.202	24.423	19.691	13.262	60.579

Table 13. Calculation results of the stator core loss.

Loss	Method 1	Method 2	Method 3
Hysteresis loss (W)	34.688	37.880	39.618
Eddy current loss (W)	17.772	19.410	20.300
Additional loss (W)	0.576	0.657	0.661
Stator core loss (W)	53.036	57.947	60.579

5. PROTOTYPE EXPERIMENT OF HEDM

To test the efficiency and loss of the ECMPDM under various working conditions, dynamometer is used to test the prototype, as shown in Figure 12.

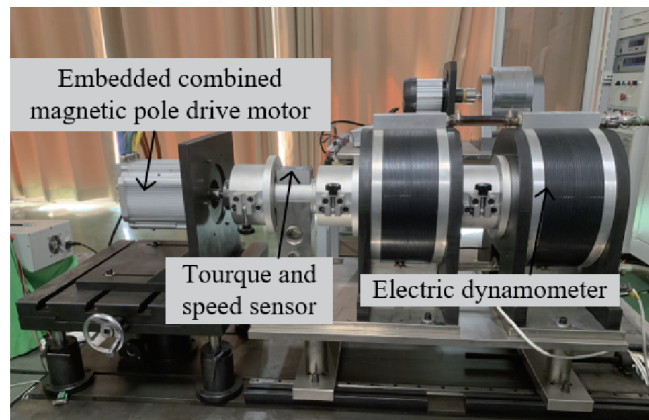


Figure 12. Experimental platform of the ECMPDM.

5.1. No-Load Core Loss Test of the ECMPDM

Using the dynamometer experimental platform, the no-load loss of the ECMPDM is tested. The no-load three-phase of the prototype is disconnected and in open circuit state; the dynamometer drives the motor under test; and the dynamometer gives the speed. At this time, the motor has no copper loss, and the eddy current loss of the permanent magnet can also be ignored. Therefore, the core loss under no-load condition can be expressed as the power minus the mechanical loss, which is detailed as follows

$$\begin{aligned}
 P_{Fe} &= \frac{n \times T_0}{9.55} - P_{ml} \\
 &= \frac{n \times T_0}{9.55} - K_b m_t n_N \times 10^{-3} + \frac{2}{3} D_{i1} l_z n_N^3 \times 10^{-3}
 \end{aligned} \tag{12}$$

where P_{Fe} is the core loss of the motor, T_0 the torque, P_{ml} the mechanical loss, K_b the frictional resistance coefficient, m_t the motor rotor mass, n_N the rated speed, D_{i1} the diameter of stator, and l_Z the axial length of stator.

Figure 13 shows the changes in core loss simulation results and experimental results with different speeds. It can be seen that with the increase of speed, the core loss of the motor is also increasing. When the speed exceeds the rated speed of 3000 r/min, the rate of core loss increases.

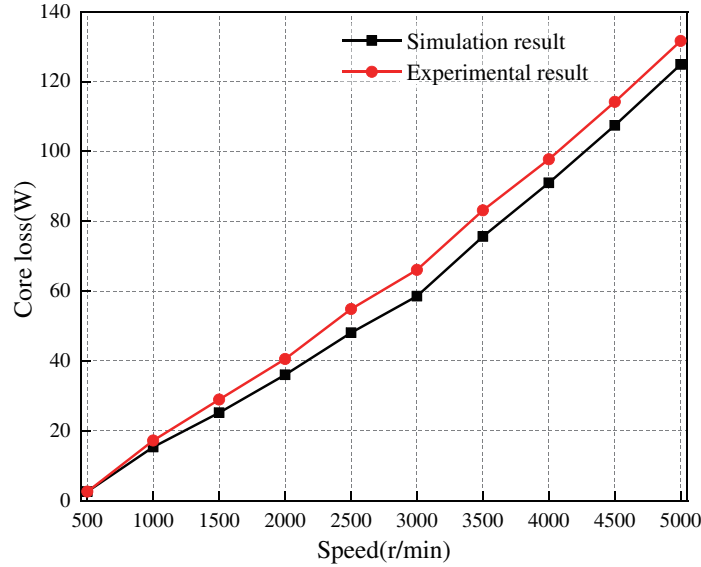


Figure 13. Simulation and test results of the core loss of drive motor.

5.2. Rated Voltage Characteristic Test of the ECMPDM

The output characteristic data of the ECMPDM at rated voltage is obtained through a dynamometer test, as shown in Figure 14. From the experimental results, the ECMPDM can maintain stable output torque and speed under rated load conditions, and the high-efficiency working range (efficiency $\geq 80\%$)

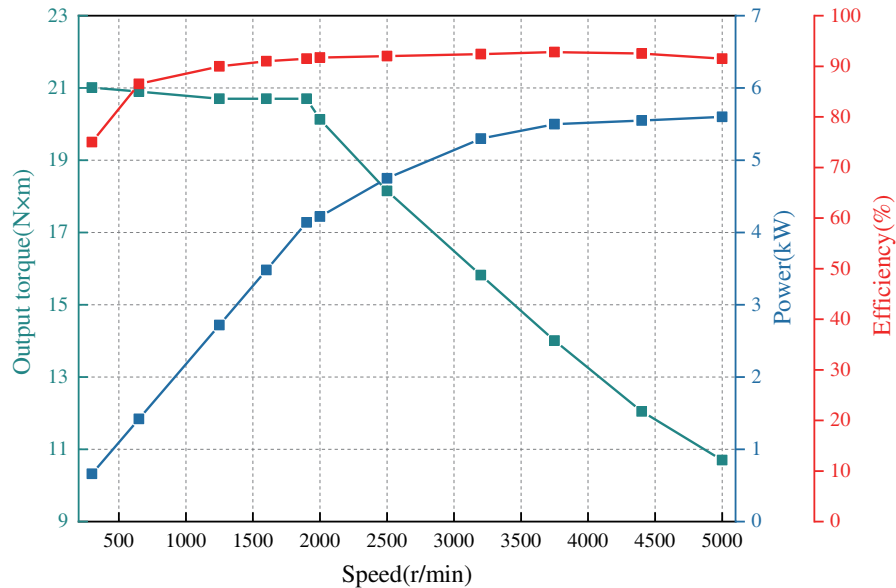


Figure 14. Rated voltage output characteristic curve of the ECMPDM.

accounts for more than 88% of the total working range. Under the rated voltage, the total loss includes not only the core loss and mechanical loss, but also the copper loss. It becomes complex to calculate the core loss separately. Therefore, the core loss of the prototype is indirectly proved to meet the design requirements through the calculation efficiency.

5.3. Peak Power Characteristic Test of the ECMPDM

Under the extreme conditions of rapid acceleration and full load climbing of electric vehicles, the driving motor needs to work overload. The peak power characteristic experiment can test the dynamic performance of the drive motor under extreme condition. Figure 15 shows the characteristics of the peak power output of the drive motor. When the drive motor is overloaded, the copper consumption increases, so the total loss increases, and the efficiency decreases. At the rated speed, the overload efficiency does not decrease much compared with the rated efficiency, which is mainly caused by the increase in copper consumption, and the value of core loss does not increase too much.

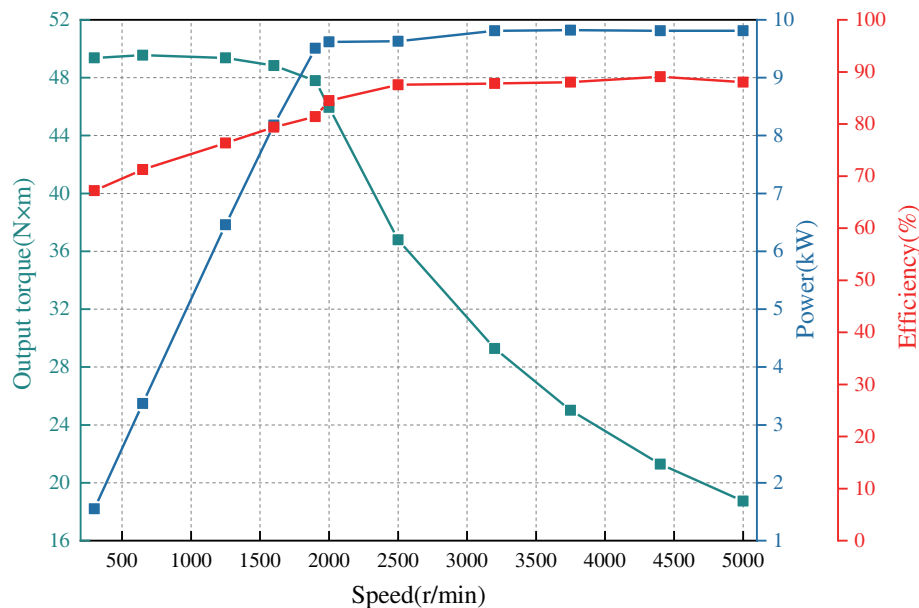


Figure 15. Peak power output characteristic curve of the ECMPDM.

Through the no-load loss test, it can be seen that the core loss test value at the rated speed is consistent with the simulation value. Through the rated voltage characteristic test and peak power test, it can be seen that the optimized motor efficiency is above 90%, and the design meets the output requirements.

6. CONCLUSION

This paper studies the influencing factors of the core loss of the ECMPDM for new energy vehicles. In addition, this paper also draws the following conclusions:

1) The mathematical model of core loss of the ECMPDM is established. According to the analysis of the mathematical model, the magnetic flux density is studied before studying the core loss; the monitoring points are selected in different areas of the stator; and the magnetic density of the selected monitoring points is analyzed to preliminarily verify the correctness of the model.

2) The stator silicon steel material and stator slot size are optimized respectively. Select four kinds of silicon steel sheet materials, DW310_35, DW315_50, DW360_50, and DW465_50; compare the stator core loss and the radial magnetic density of point B of the four materials; and select the best silicon

steel sheet material. The response surface analysis method is used to optimize the stator slot size. The radial magnetic density amplitude of point B and the average stator core loss are selected as the two optimization objectives. By solving the relationship between the two optimization objectives and the design value, the Pareto front distribution diagram is obtained, and the optimal solution of the optimization model is selected.

3) DW310.35 is selected as stator silicon steel material. The final variables of stator slot size are H_{s0} , H_{s1} , H_{s2} , B_{s0} , B_{s1} , and B_{s2} , whose values are 0.87 mm, 0.69 mm, 13.78 mm, 2.38 mm, 3.83 mm, and 4.51 mm, respectively. The optimal stator structure is analyzed, and the stator core loss is calculated by three methods. The core loss value obtained by method 2 is the closest to the simulation value.

4) The prototype is made, and the no-load core loss test, rated voltage characteristic test, and peak power characteristic test are carried out, respectively. The correctness of the simulation value under no-load conditions is verified through the no-load test. The rated voltage characteristic test and peak power characteristic test indirectly verify that the core loss value will increase with the increase of speed.

7. DATA AVAILABILITY

All data used to support the findings of this study are available from the corresponding author upon request.

8. CONFLICTS OF INTEREST

The authors declare that there is no conflict of interest regarding the publication of this paper.

ACKNOWLEDGMENT

This research was supported by the National Natural Science Foundation of China (Grant No. 52275261 and 51975340).

REFERENCES

1. Ludmila, L. and D. Janis, "Comparison of permanent magnet synchronous motor and synchronous reluctance motor based on their torque per unit volume," *2014 Electric Power Quality and Supply Reliability Conference (PQ), IEEE*, 233–236, 2014.
2. Li, L. J., S. H. Li, G. M. Li, et al., "Design and performance prediction of switched reluctance motor with amorphous cores," *Materials Research Innovations*, Vol. 19, Sup. 3, S28–S32, 2015.
3. Dong, J. N., Y. K. Huang, L. Jin, and H. Y. Lin, "Review on high speed permanent magnet machines including design and analysis technologies," *Proceedings of the Chinese Society of Electrical Engineering*, Vol. 34, No. 27, 4640–4653, 2014.
4. Li, Q., T. Fan, and X. H. Wen, "Stator teeth eddy-current loss analysis of interior permanent magnet machine during flux weakening," *International Conference on Electrical Machines and Systems*, 1226–1230, 2013.
5. Li, Q., T. Fan, and X. H. Wen, "Armature-reaction magnetic field analysis for interior permanent magnet motor based on winding function theory," *IEEE Transactions on Magnetics*, Vol. 49, No. 3, 1193–1201, 2013.
6. Li, Q., T. Fan, and X. H. Wen, "An improved model of estimating core loss for interior permanent magnet synchronous machine," *IEEE Vehicle Power and Propulsion Conference*, 169–173, 2013.
7. Mi, C., G. R. Slemon, and R. Bonert, "Modeling of core losses of surface-mounted permanent magnet synchronous motors," *IEEE Industry Applications Society*, Vol. 4, 2585–2591, 2001.
8. Feng, Y. L. and C. N. Zhang, "Core loss analysis of interior permanent magnet synchronous machines under SVPWM excitation with considering saturation," *Energies*, Vol. 10, No. 11, 2017.

9. Naoya, S. and M. Enokizono, "Stator core shape design for low core loss and high power density of a small surface-mounted permanent motor," *Sensors (Switzerland)*, Vol. 20, No. 5, 2020.
10. Tao, D. J., K. L. Zhou, F. Lv, et al., "Magnetic field characteristics and stator core losses of high-speed permanent magnet synchronous motors," *Energies*, Vol. 13, No. 3, 2020.
11. Zhao, H. S., Y. L. Luo, X. F. Liu, R. H. Wang, and W. H. Chen, "Analysis on no-load core losses distribution of asynchronous motors with time-stepping finite element method," *Proceedings of the Chinese Society of Electrical Engineering*, Vol. 30, No. 30, 99–106, 2010.
12. Wan, Z. Y., D. Y. Fan, X. Y. Zhu, X. Zhou, Z. X. Xiang, and L. Quan, "Research on core loss characteristics of a high-efficiency light-weight variable-leakage-flux permanent magnet motor considering multiple operation conditions," *Proceedings of the Chinese Society of Electrical Engineering*, 1–8, 2022.
13. Bertotti, G., "General properties of power losses in soft ferromagnetic materials," *IEEE Transactions on Magnetics*, Vol. 24, No. 1, 621–630, 1987.
14. Ma, S. Q., B. Yuan, Z. F. Xin, and Y. B. Sun, "Calculation and finite element analysis of surface mounted permanent magnet synchronous motor core loss based on FLUX," *Journal of Dalian Jiaotong University*, Vol. 38, No. 5, 65–69, 2017.
15. Zhao, G. X., D. C. Kong, and X. L. Gao, "Performance difference study on permanent magnet synchronous motor based on soft magnetic composite material and silicon steel sheet," *Transactions of China Electrotechnical Society*, Vol. 33, Sup. 1, 175–181, 2018.
16. Liang, L. M., Y. F. Zeng, D. S. Liu, and W. S. Zeng, "The impact of different stator core material on core losses of permanent magnet synchronous motor," *Manufacturing Automation*, Vol. 40, No. 4, 148–152, 2018.
17. Yoon, K. Y. and K. Y. Hwang, "Optimal design of spoke-type IPM motor allowing irreversible demagnetization to minimize PM weight," *IEEE Access*, Vol. 9, 65721–65729, 2021.
18. Du, L., L. Y. Lv, W. Sun, and X. G. Song, "An Latin hypercube sampling approach for constrained design space," *Machinery Design & Manufacture*, No. 8, 43–47, 2021.
19. Zhang, Z. Y., C. X. Jiao, T. Sang, and Q. X. Zhang, "Latin hypercube sampling simulation of response surface model parameters of vehicle body," *Computer Simulation*, Vol. 38, No. 7, 123–127, 2021.
20. Saleem, M. and A. Hosoda, "Latin Hypercube sensitivity analysis and Non-destructive test to evaluate the pull-out strength of steel anchor bolts embedded in concrete," *Construction and Building Materials*, Vol. 290, No. 5, Article ID 123256, 2021.
21. Hu, X. B., S. H. Gu, C. Zhang, et al., "Finding all Pareto optimal paths by simulating ripple relay race in multi-objective networks," *Swarm and Evolutionary Computation*, Vol. 64, No. 1, Article ID 100908, 2021.
22. Wei, M., M. Zhang, Y. Zhu, et al., "Analysis and optimization of a new 2-D magnet array for planar motor," *IEEE Transactions on Magnetics*, Vol. 46, No. 5, 1167–1171, 2010.